ADVANCED MATERIALS
www.advmat.de

Identification of Facet-Governing Reactivity in Hematite for Oxygen Evolution

*Hao Wu, Tong Yang, Yonghua Du, Lei Shen, and Ghim Wei Ho**

Unveiling the impact of a single parameter on the catalytic descriptor is fundamental to guide rational design principles for high-activity catalysts. Facets with distinct surface coordination that exhibit a central role in the kinetics modulation (reactivity) of surface electrochemistry, have remained elusive in oxygen evolution reactions (OERs). Here, the relationship between the predominant facets and catalytic reactivity is revealed, and it is recognized that facets decisively govern the oxygen evolution activity descriptor in hematite nanocrystals. Specifically, the hematite shows facet-dependent activity that follows the computed binding energy of surface-oxygenated intermediates. Moreover, a lower kinetics energy barrier is observed on a highly coordinated surface, both experimentally and computationally, in the light of molecular orbital principles. Consequently, a record-low overpotential and Tafel slope in iron oxides toward OER are manifested, competing against the benchmark binary transition metal oxide electrocatalysts and expelling the stereotype of the passive oxygen evolution activity of iron oxides. Significantly, the identification of facet-governing reactivity, construction of favorable facets, and strategic regulation of surface covalency enlighten design strategies for highly active catalysts.

Dr. H. Wu, Prof. G. W. Ho
Department of Electrical and Computer Engineering
National University of Singapore
117583, Singapore
E-mail: elehgw@nus.edu.sg
Dr. H. Wu, Prof. G. W. Ho
Engineering Science Programme
National University of Singapore
117575, Singapore
Dr. H. Wu, Prof. G. W. Ho
Institute of Materials Research and Engineering
A*STAR (Agency for Science, Technology and Research)
117602, Singapore
T. Yang, Prof. L. Shen
Department of Physics
Faculty of Science
National University of Singapore
117551, Singapore
Dr. Y. Du
Department of Mechanical Engineering
Engineering Science Programme
Faculty of Engineering
National University of Singapore
117575, Singapore
The ORCID identification number(s) for the author(s) of this article can be found under https://doi.org/10.1002/adma.201804341.

DOI: 10.1002/adma.201804341

Oxygen evolution reaction (OER) is of essence to the electrochemical renewable fuels generation in water electrolysis and CO_2 reduction configurations, and energy storage in metal–air batteries.[1] Typically, this half-reaction requires high overpotentials due to the sluggish kinetics in the intricate four-electron redox processes at the anode.[2] Exploring highly-active, robust, and resource-abundant OER electrocatalyst alternatives to the state-of-the-art noble-metal-based (e.g., Ru, Ir) ones for efficient electrolyzers is highly motivated yet challenging.[3–5] Earth-abundant first-row 3d transition metal oxides (TMOs), especially the Co, Ni, and Mn based ones are expected to qualify as the substitutes due to their high tunability of the OER activity descriptors (e.g., the e_g orbital occupancy of transition metal ions in perovskites; coordinatively unsaturated metal cation of TMOs).[6–8] Iron oxide (e.g., α-Fe_2O_3), as one of the most stable, cost-effective and environment-friendly TMOs, has been widely investigated as a light absorber for water oxidation, but suffers from the sluggish kinetics of the interfacial extraction of holes.[6g] The feasible manipulability of size and surface atomic arrangement renders it a tempting OER electrocatalyst. By far, predictably most of the given binary TMOs have made little headway in reaching the summit of the OER volcano plots (theoretical overpotential as a function of $\Delta G_{O*} - \Delta G_{OH*}$ by density functional theory (DFT) calculations) that follow the Sabatier principle.[9,10] To address this issue, established strategies have been implemented, such as electronic structure/interaction modulation, intermediates adsorption fine-tuning, lattice-oxygen participation and geometry engineering as well as conductivity improvement, by means of elemental doping, component coupling, vacancy inclusion, and the synergetic influence of supports, etc.[11,12] Nevertheless, such complex alternatives inevitably brings grand challenges to the fundamental understanding, though advanced spectroscopy and rational computational theory have been developed to predict fairly accurately.[13] Worse, ambiguous active sites identification and even contradictory catalytic trends have been reported, leading to inconclusive intrinsic descriptors for substantial implementation of the electrolyzer.[14] The contribution of all-sided single parameter to the OER activity is, therefore, of great urgency to be uncovered, so as to guide rationally the design principles of high intrinsic activity of OER catalysts.

Beyond the composition manipulation tactic, crystal-facet engineering plays a central role in the kinetics modulation of the redox reactions on the catalyst surface.[15] Generally, high-active facets correspond to high-index facets that are endowed with favorable atomic arrangement, termination, and coordination.[16] Benefiting from such amelioration, superior activities have been realized readily in noble metals and alloys, as well as metal oxides toward (photo)electrochemical catalysis, photovoltaic devices and lithium–oxygen batteries, and so on.[16,17] Yet, this has rarely been demonstrated for OER, and indeed, theoretical OER overpotential calculations of binary TMOs are rarely crystal-facet specific, if ever, the size effects have not been eliminated completely.[17] Thus, the impact of facets on OER descriptor is mostly neglected and not clarified, leaving unsubstantial relationship between predominantly exposed facets and catalytic reactivity. This, to a large extent, is due to prevailing elimination or dissolution of the high-index facet during the crystal growth process to compromise the thermodynamic stability.[18–20] Intrinsically, the high-indexed facets have high surface energy, while the growth crystallite supersaturation, in proportion to the surface energy, decreases gradually under the conventional synthetic conditions, resulting in diminished high-index facets.[18,19] Though crystals with high-index facets could be achieved using surfactant-capping, and template or ion-directed implantation in the facet-controlled synthesis, the end products are inevitably encapsulated with undesirable surfactant molecules or complex moieties such that the surface-dominant reactivity would be deactivated.[20] Thereby, the expression of "facet-determining activity" may not be explicitly unequivocal. Thus, the role of facet on the OER activity of binary TMOs needs to be elucidated, which is essentially fundamental to the rational design of exceedingly active and stable electrocatalysts.

Herein, we explicitly unveil facet as the key determining factor that defines the reactivity of binary hematite (α-Fe_2O_3), in which well-crafted nanocrystals show facet-dependent OER activities. The champion catalyst, corresponding to the high-indexed (012) facet nanocrystal, can be exclusively realized by an unconventional acid-etching strategy that is designed to suppress the decrease of the growth crystallite supersaturation that happens readily in the classical thermodynamically favored crystal growth. DFT calculations suggest the trend of adsorption energy difference (ΔG) of intermediates; hence, the theoretical OER overpotential matches with the experimental results. X-ray absorption near edge structure (XANES) studies reveal that the pristine acid-etched nanocrystal is of high covalent bonding (seven-coordination), which can be varied optionally to a common six-coordination for impartial comparison. A lower kinetics energy barrier is observed both experimentally and computationally on the seven-coordinated surface, which is ascribed to the decrement of e_g occupancy of the Fe 3d orbital in the light of molecular orbital principles. Significantly, the viable etching and identification of facet-governing OER reactivity in hematite, and construction of high covalency surfaces to strengthen the relatively weak intermediate binding open up new tunability to reconfigure inactive catalyst with augmented electrochemical activity.

To exclude the impact of size and surface impurities on the reactivity, three kinds of hematite with similar size were

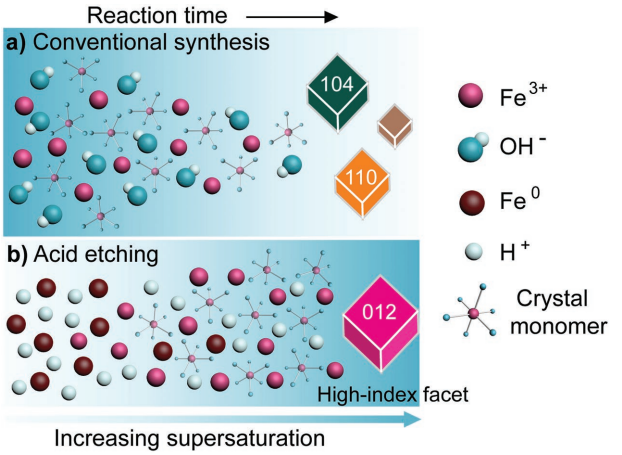

Figure 1. Schematic of crystal monomer supersaturation regulation. a) Supersaturation decreases in conventional synthesis. b) Supersaturation increases in unconventional acid-etching process.

synthesized, such that the difference between them is predominantly the exposed facet. We adopted modified solvothermal and hydrothermal methods to fabricate the respective (104) and (110) facet exposed nanocrystals (see details in Experimental Section). The crystal monomer supersaturation decreases gradually in the conventional growth processes, as schematically depicted in **Figure 1**a. According to the Thomson–Gibbs equation, the supersaturation is in proportion of crystal surface energy. Thus, the high-index facets with high surface energy would diminish eventually as the reaction proceeds. Previous reports have increased the supersaturation of the crystal growth monomers or applied ions-directing to realize high-index, e.g., (012) facet exposed α-Fe_2O_3 nanocrystals.[18] Yet, undesired organic additive (oleic acid) or foreign ions are unavoidable, and worse, accompanied by vast oxygen vacancies, hence impeding a rigorous comparison between the hematite. Recently, we successfully developed an unconventional acid-etching strategy to suppress the cation hydrolysis by releasing varied cations.[21,22] Inspired by this ability, the synthetic reconditioning is expected to sustain the iron cations in acidic media; thus, maintaining the supersaturation, as conceptualized in Figure 1b. Subsequently, we adopted the unconventional acid-etching strategy (see Experimental Section) to control the cations releasing, so as to hold the supersaturation of the growth monomers, and finally lead to high-index (012) facet crystals.

First, the composition of the end products obtained through unconventional acid-etching strategy and the conventional solvothermal and hydrothermal methods were identified by X-ray diffraction (XRD) characterization. All three resultant nanocrystals match with the pure hexagonal hematite (α-Fe_2O_3, PDF no. 33–0664), as shown in **Figure 2**a. The structure of the as-prepared nanocrystals was then revealed by scanning electron microscopy (SEM), where all samples show uniform morphology (Figures S1–S3, Supporting Information). Subsequently, transmission electron microscope (TEM) was used to visualize the geometrical features and exposed facets of the three hematite nanocrystals. The acid-etched ones are structurally well-defined and monodispersed with a uniform lateral size ranging from 80 to 90 nm (Figure 2b and inset). The selected-area electron diffraction (SAED) pattern suggests that

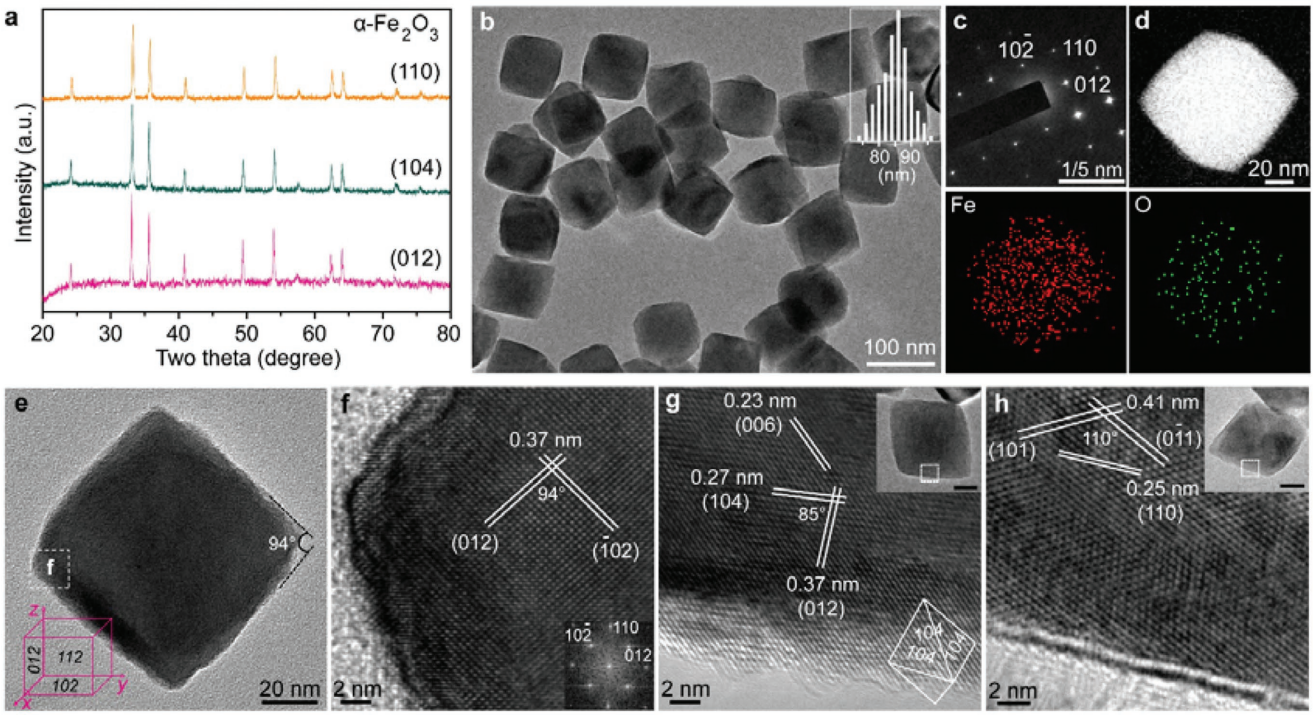

Figure 2. Composition and structure characterization. a) XRD patterns of the three nanocrystals. b) TEM image of acid-etched nanocrystals. Inset, size distribution. c) SAED pattern of an acid-etched nanocrystal. d) Scanning TEM image and elemental mapping of Fe and O. e) A representative TEM image of the acid-etched nanocrystal. Inset, geometrical model. f) HRTEM image of the acid-etched nanocrystal. Inset, corresponding FFT. g) HRTEM image of the solvothermal nanocrystal. Inset, a representative TEM image and geometrical model. h) HRTEM image of the hydrothermal nanocrystal. Inset, a representative TEM image. The scale bars of insets in (g) and (h) are 20 nm.

the acid-etched nanocrystal is of single crystallinity with two sets of interplanar spacing that belong to (012) and (110) planes (Figure 2c). Energy dispersive X-ray spectroscopy (EDS) visualizes the homogeneous distributions of Fe and O elements with a molar ratio of ≈2:3 in the nanocrystal (Figure 2d; Figure S4, Supporting Information). A typical TEM image reveals a dihedral angle of 94° (Figure 2e), featuring two sets of consistent lattice spacing of 0.37 nm that belongs to (012) plane revealed by high-resolution TEM (HRTEM) (Figure 2f; Figure S5, Supporting Information). The corresponding fast Fourier transform (FFT) pattern matches with the SAED. The geometrical model of the nanocrystal is in good agreement with the ideal rhombohedron enclosed by (012) facets (in three-index notation).[23] The nanocrystal through the solvothermal method presents a trigonal bipyramidal geometry (inset of Figure 2g), with lattice fringes of 0.37, 0.27, and 0.23 nm, corresponding to the (012), (0-14), and (006) planes. The measured interfacial angle between the (0-14) and (012) indices is about 85°, in accordance with the nanocrystal enclosed by all (104) facets (Figure 2g; Figure S6, Supporting Information).[23] As for the hydrothermal one, TEM shows interplanar fringe of 0.41 nm (110° in angle), in agreement with the (101) and (0-11) crystal planes, and the 0.25 nm, corresponding to the (110) lattice plane. The geometrical features indicate that the nanocrystals are enclosed by the (110) facets (Figure 2h; Figure S7, Supporting Information).[23] Notably, crystal with high-indexed (012) facet is realized by the acid-etching strategy, while it is hardly achievable through conventional hydro/solvothermal methods.[18,19]

To reveal the formation mechanism, the morphology evolution of the acid-etched nanocrystals was recorded at different reaction periods, where numerous small crystal seeds were formed in the initial stage (5 h), which gradually grew in size, and finally formed monodispersed crystals after 20 h (Figure S8, Supporting Information). The acid-etching strategy probably follows the classic nucleation and growth process, such that the crystal monomer supersaturation is the primary driving force for both conventional and acid-etching routes. During conventional growth, iron cations and hydroxyls are consumed gradually as the hydrolysis and pyrolysis proceed, leading to the decrease of pH and monomer supersaturation. For acid-etching, protons are consumed to oxidize metallic iron to cations, part of which is involved in the generation of crystal monomers, leading to the increase of pH. Iron cations could still be released in a relatively acidic condition, thus providing sustained supersaturation of crystal growth monomers. As the consumption of protons progresses (50 h), limited iron cations and thus crystal monomers are formed, resulting in the merging of the crystals for the reduction of the surface energy (Figure S9, Supporting Information). These presumptions are verified by the measured pH values during the reactions of both conventional hydro/solvothermal methods and unconventional acid-etching strategy (Table S1, Supporting Information). Thus, it is the suppression of the supersaturation decrement that leads to the formation of uncommon high-index facet crystals in the acid-etching process.

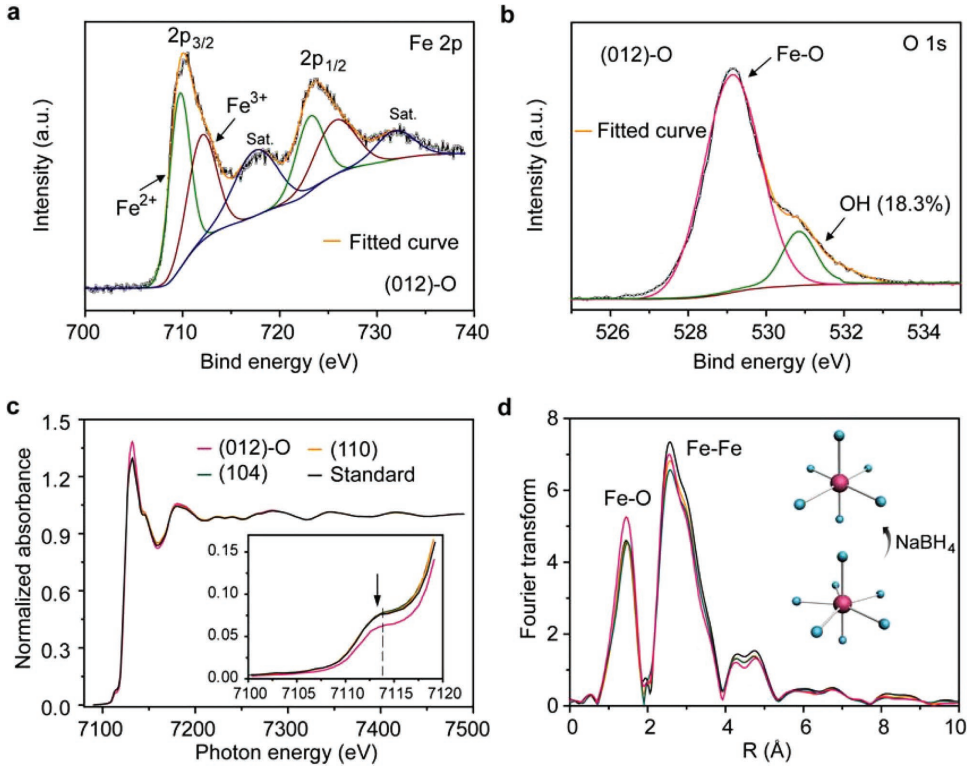

Figure 3. Electronic structure investigation. a,b) XPS spectra of Fe 2p (a) and O1s (b) of acid-etched nanocrystals. c) XANES spectra of the three nanocrystals and standard hematite. d) FT of EXAFS. Inset, schematic diagram of six- and seven-coordinated configurations.

The elemental valence states were examined using X-ray photoelectron spectroscopy (XPS), as shown in **Figure 3**a,b. For acid-etched nanocrystal, the main deconvoluted peaks located at 711.1 and 725.4 eV correspond to the trivalent Fe 2p3/2 and 2p1/2, along with two minor ferrous peaks and satellite indication. Negligible differences between the Fe spectra are detected for the three samples (Figure S10, Supporting Information). Yet, as for the O1s peak, the acid-etched nanocrystal shows a quite distinct feature, where a much higher ratio (15.1%) of deconvoluted hydroxyl peak centered at 531.1 eV is observed,[4] in comparison to the solvothermal (12.5%) and hydrothermal (4.6%) ones (Figure S11, Supporting Information). There is no peak shift observed for O1s, thus the oxygen vacancy effect is excluded from consideration. These features are consistent with the XRD results, confirming that the predominant composition is α-Fe_2O_3 for all three crystals, but probably with distinctive surface bonding terminations. To reveal the local bonding environment, Fe K-edge XANES spectra were examined. As shown in Figure 3c, the curves of both solvothermal and hydrothermal α-Fe_2O_3 nanocrystals almost overlap with that of the reference standard α-Fe_2O_3 powder, while the acid-etched one exhibits an obviously lower intensity in terms of pre-edge peak at around 7114 eV, indicating a higher local oxygen coordination of the Fe atoms.[5] The corresponding Fourier transforms (FT) of extended X-ray absorption fine structure (EXAFS), as a function of the interatomic distance, were plotted and fitted using FEFFIT program to reveal the local atomic and electronic structure (Figure S12 and Table S2, Supporting Information). As depicted in Figure 3d, the first peak located at 1.4 Å represents the first coordination shell of the Fe atom, ascribing to the Fe—O scattering paths. The average coordination number for solvothermal and hydrothermal nanocrystals are quantitatively analyzed, which are approximately six, indicating a typical octahedral-coordinated Fe—O bonding that is consistent with the standard α-Fe_2O_3 (inset of Figure 3d). Notably, the acid-etched nanocrystal exhibits an enhanced Fe—O peak with increased coordination numbers close to seven, implying a pentagonal bipyramidal geometry of Fe—O bonding. The increase in the coordination number of the acid-etched sample is in agreement with the high intensity of adsorbed hydroxyl in the XPS results. To rigorously explore the facet impact on OER activities, the hydroxyl terminations on the (012) surface are to be eliminated so as to obtain a common octahedral coordination. The as-obtained acid-etched sample was treated with $NaBH_4$ (see Experimental Section), and subsequently examined by XPS and XANES spectra. It is observed that the Fe retains trivalence, while the hydroxyl proportion is dramatically decreased (11.7%) after $NaBH_4$ treatment (Figure S13, Supporting Information). Significantly, the intensity of pre-edge peak is increased approximately to that of the standard α-Fe_2O_3 powder and the fitted coordination number is closed to six, confirming the commonly coordinated (012) facet of the $NaBH_4$-treated sample (Figure S14, Supporting Information). Hereafter, the acid-etched nanocrystals before and after $NaBH_4$ treatment are denoted as (012)-O and (012), while the solvothermal and hydrothermal ones are designated by the preferentially exposed facets, i.e., the (104) and (110), respectively.

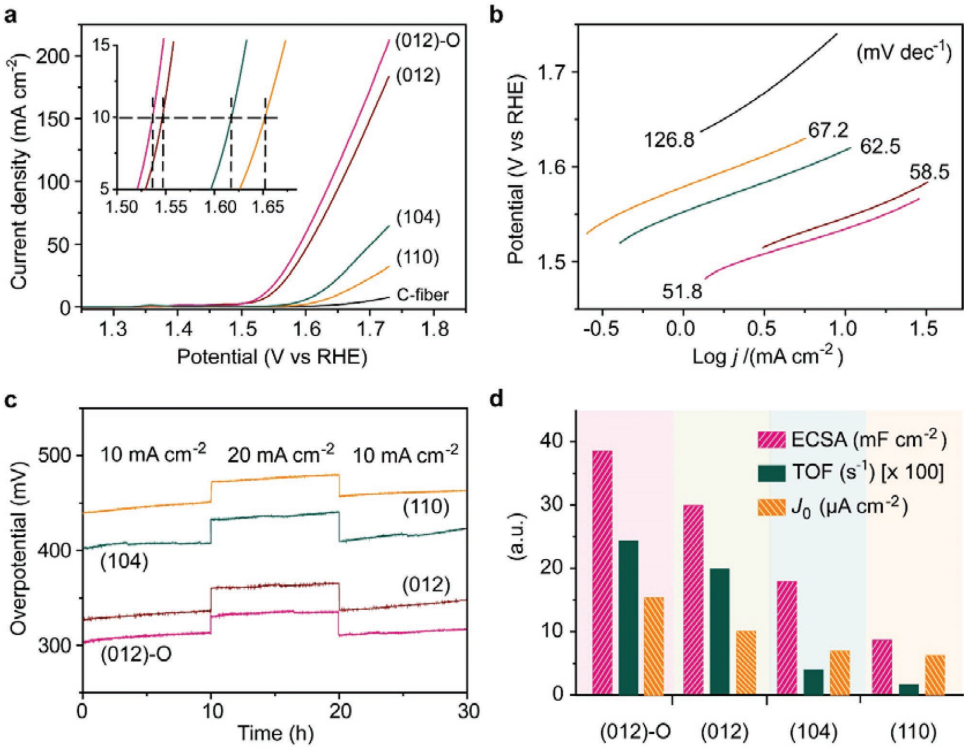

Figure 4. Evaluation of oxygen evolution reactivity. a) OER polarization curves and b) corresponding Tafel slopes of the four electrodes and C-fiber substrate. c) Galvanostatic stability measurements. d) ECSA, TOF, and J_0 comparison.

Electrodes were fabricated using the (012)-O, (012), (104), and (110) α-Fe_2O_3 nanocrystals as active materials on C-fiber cloth to evaluate the OER performance (see Experimental Section for details). These nanocrystals were fairly monolayer dispersed over the C-fiber (Figure S15, Supporting Information). The bare C-fiber, as the current collector, shows negligible contribution to the polarized current (**Figure 4**a). Distinctly, the (012) electrode exhibits predominant OER activities with much higher current densities (e.g., 93.4 mA cm^{-2} at 1.65 V) than that of the (104) and (110) ones (22.7 and 9.6 mA cm^{-2}, respectively), as depicted in the polarization curves. A lower overpotential of 317 mV at 10 mA cm^{-2} is observed for the (012) electrode, compared to 388 mV for the (104) and 422 mV for (110) one, respectively. Accordingly, the (012) electrode shows the lowest extracted Tafel slope of 58.5 mV dec^{-1} among the three electrodes (Figure 4b). Interestingly, the facet, being one and only different criterion among them, displays a great influence on the OER activities in hematite. As such, the nanocrystal with high-index exposed facet exhibits the highest OER performances, which is highly competitive to the benchmark binary TMO electrocatalysts, hence expelling the prejudices and stereotypes of the passive OER activity of iron oxides.[24] Moreover, the acid-etched nanocrystals at different periods are examined, among which the 20 h one shows the best performance toward OER (Figure S16, Supporting Information). This can be explained by the sufficient presence of the high-index facets exposure. Specifically, the high-index facets have not been appreciably formed in the initial stage (within 10 h), while extended crystal agglomeration occurs with the decrease of growth supersaturation in the posterior process (after 30 h), which render poor OER performance. Additionally, to exclude the inaccuracy of the reference electrode, OER polarization curve was examined using Ag/AgCl as reference electrode. Negligible difference with either the Hg/HgO or Ag/AgCl as reference electrode, and with either C-fiber or Ni foam as current collector are detected, indicating the reliable OER behaviors of the (012) electrode (Figure S17, Supporting Information). Notably, the pristine (012)-O with seven-coordinated Fe—O bonding displays slightly higher OER activities in terms of overpotential (305 mV) and Tafel slope (51.8 mV dec^{-1}). This could be explained by the decreased e_g occupancy of the surface Fe antibonding orbitals. Specifically, in the octahedral-coordinated configuration, the high e_g occupancy of 2 is too high, rendering the binding of oxygen intermediates too weak (Figure S18, Supporting Information).[8,9] The e_g occupancy is, however, reduced in the high covalent Fe orbital, which will strengthen the weak bonding of the OER intermediates and thus enhance the intrinsic OER activities. The stability of the electrodes was evaluated with galvanostatic measurements, as recorded in the chronopotentiometric curves (Figure 4c). XANES spectrum and corresponding FT show negligible change after OER test, indicating the steady surface bonding of the $NaBH_4$-treated nanocrystals (Figure S19 and Table S2, Supporting Information). Furthermore, no surface reconstruction is observed in the nanocrystals (Figure S20, Supporting Information), implying the sturdy chemical bonds on the surface. The increment of overpotential for (012)-O, (012), (104), and (110) electrodes after a consecutive operation of 30 h are about 14, 20, 21, and 24 mV respectively, indicating the high durability for all nanocrystals in the alkaline media.

The criteria for evaluating the OER activity, including the electrochemical surface area (ECSA) and turnover frequency (TOF) as well as exchange current density (J_0), were measured and is summarized in Figure 4d. The ECSAs were estimated by the double-layer capacitances, which were derived from the cyclic voltammetry (CV) at non-Faradaic potential window by fitting the linear slopes (Figures S21 and S22, Supporting Information).[21,22] Evidently, the (012) electrode exhibits a high ECSA (29.8 mF cm^{-2}), 1.7-fold and 3.5-fold of the (104) and (110) ones, implying more accessible active sites. The TOFs were calculated to quantify the specific activity of OER for all samples, in which the value for the (012) electrode is estimated to be 0.197 s^{-1}, 4-fold and 11-fold higher than that of the (104) and (110) ones. The predominant TOF of the (012) nanocrystals ensures high specific activity on the active sites. The J_0, reflecting the intrinsic rate of redox reaction, were extracted by extrapolating the Tafel slopes (Table S3, Supporting Information).[22] A higher J_0 of 8.3 μA cm^{-2} is observed for the (012) sample compared to 6.9 μA cm^{-2} for (104) and 6.2 μA cm^{-2} for (110), suggesting an intrinsically fast water oxidation reaction. These parameters of the (012)-O electrode are higher than that of the (012) one, demonstrating an exceptional electrocatalyst toward OER. In addition, the interfacial charge transfer resistance (R_{ct}) under OER-operating conditions were studied by the electrochemical impedance spectroscopy (EIS) and quantified by fitting the Nyquist plots with equivalent circuits (Figure S23, Supporting Information). The R_{ct} values for the electrodes are comparable, though the (012) one is a little smaller than that of the others. Besides, there is little difference of the surface potential difference between the electrodes, revealing a comparable electron–hole recombination rate (Figure S24 and Table S4, Supporting Information). Thus, the charge transfer kinetics of the electrode would not dominate the OER activity. These experimental results clearly signify that distinct catalytic performances are testified on different facets and coordinated surfaces, indicating contrasting kinetics energy barriers, which are to be uncovered computationally.

DFT computations of the free energy for all intermediates in OER steps (see Experimental Section and Supporting Information) were conducted to reveal the correlation between the facets and OER activities. **Figure 5**a shows the optimized atomic structures of the (012), (104), and (110) facets, as well

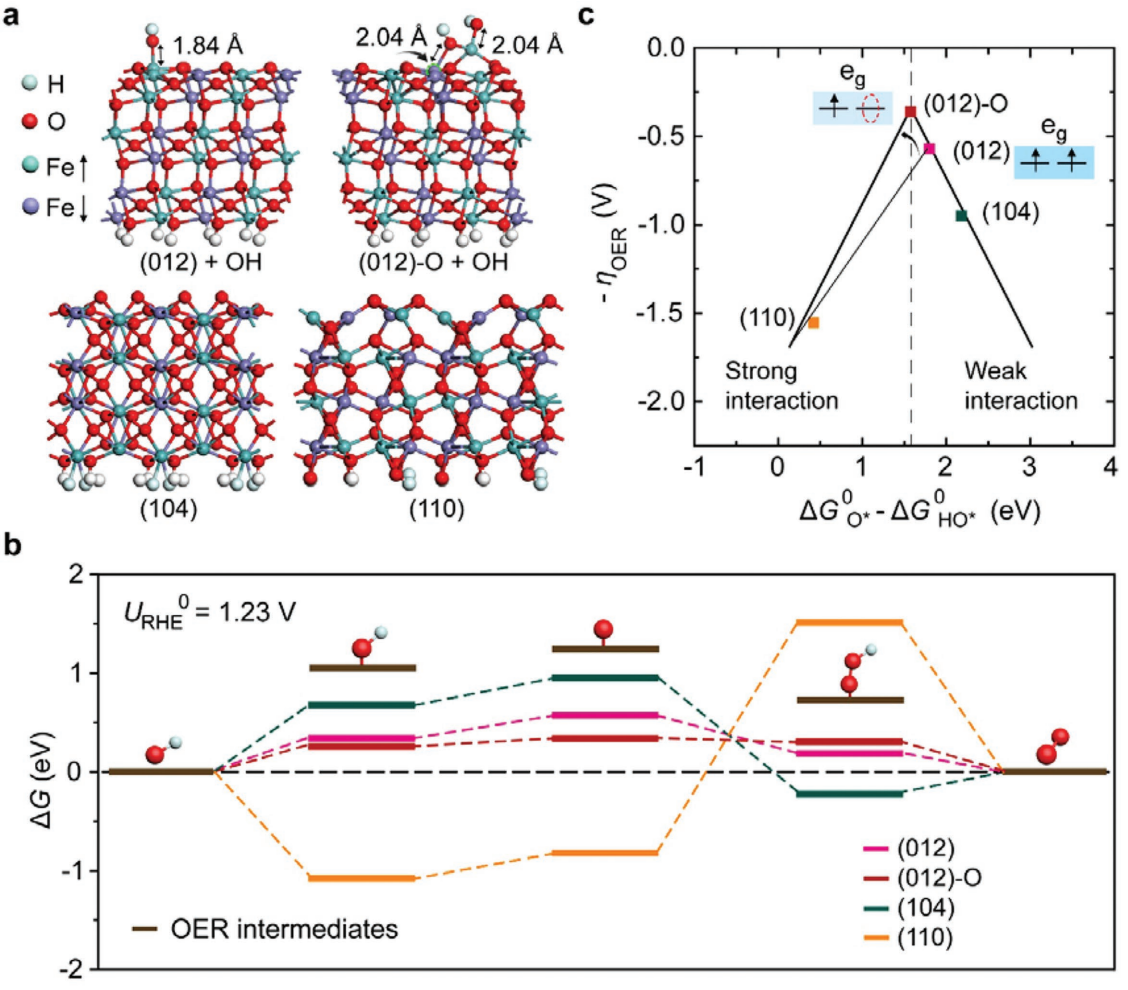

Figure 5. OER free energy diagram and identification of facet-governing reactivity. a) Optimized atomic structures for OH binding. b) Free energy diagram of OER intermediates. c) Impact of facets on the OER activity descriptor. Inset, e_g occupancy of six- and seven-coordinated configurations.

as the seven-coordinated (012)-O whose Fe—O bonds are elongated (1.84–2.04 Å) due to the interaction of the extra hydroxyls, indicating that the surface atomic arrangement greatly affects the bonding of the surface-oxygenated intermediates. Accordingly, the free energy diagram at an equilibrium potential ($U_{RHE}{}^0$ = 1.23 V, see Computational Section in Supporting Information) for the overall OER pathway is depicted in Figure 5b. As illustrated, large positive ΔG_{HO*} and ΔG_{O*} are observed on (104) facet, suggesting the adsorption of the two intermediates (HO* and O*) are too weak, which means a relatively high potential is needed to oxidize the HO* intermediate. The ΔG_{HO*} and ΔG_{O*} on (110) facet, on the contrary, are too negative, demonstrating excessively strong interaction with HO* and O* species, leading to a marked uphill formation for the subsequent HOO* intermediate. In contrast, a relatively low value of $|\Delta G|$ for all oxygenated intermediates is shown on the (012) facet, illustrating a favorable intermediary adsorption/desorption, thus a low kinetics barrier for OER. Explicitly, the distinct energetic modulations verify that the OER activities are strongly related to the predominantly exposed facets in hematite. Additionally, in the unconventional (012)-O case, it is calculated that the bonding hydroxyls are preferably co-coordinated with the neighbor Fe sites of the seven-coordinated Fe centers, resulting in elongated Fe-O bonds, which further strengthens the weak bonding of HO* and subsequent O* intermediates in the OER steps. This follows the well-established near-unity e_g occupancy descriptor, which is steadily applicable to perovskites.[7,8] The orbital principles deem that high e_g occupancy (two in the Fe 3d orbital in the conventional octahedral-coordinated Fe—O configuration) results in extremely weak bonding of oxygenated intermediates, while the reduction of which (one in the seven-coordinated Fe—O arrangement) would strengthen the weak bonding, and thus facilitate the OER kinetics.

Previously, the identification of the approximately constant scaling relation between HO* and HOO* ($\Delta G_{HOO*} - \Delta G_{HO*}$ = 3.2 ± 0.2 eV), and hence the universal OER activity descriptor, i.e., $\Delta G_{O*} - \Delta G_{HO*}$, has rationally guided the design strategies for many active catalysts.[21] The theoretical calculations are, however, impractical to take exhaustive influential factors into consideration, due to the extensive database of the surfaces over broad classes of TMOs. In this context, the unraveling of the impact of facets, with distinct atomic arrangement, termination, and coordination, on OER activity for the binary TMOs, is the key enabling step to establish the relationship between the predominantly exposed facets and catalytic reactivity. As the associated free energy diagrams for overall OER step were produced by the computations, the theoretical overpotential η_{OER} as a function of $\Delta G_{O*} - \Delta G_{HO*}$ for the hematite nanocrystals were plotted, as displayed in Figure 5c. Evidently, the activity trends toward OER show volcano-shaped relationship with the facets that follows the Sabatier principle, indicating that the facets substantially govern the universal $\Delta G_{O*} - \Delta G_{HO*}$ descriptor in hematite. Specifically, the hematite nanocrystals with predominant (110) facet interacts too strongly with the oxygenated intermediates, while the (104) facet has too weak interaction with the species, both of which result in unfavorable oxygen evolution. In contrast, the (012) facet is judiciously located at an optimal adsorption/desorption position, leading to favorable OER behavior. Besides, the optimized interaction with OER intermediates is observed on the surface with lowered antibonding Fe 3d orbitals (inset of Figure 5c), which follows the design principle of e_g occupancy descriptor based on the molecular orbital bonding framework.

In summary, we have adopted a newly proposed acid-etching strategy to realize an unconventional high-index (012) facet hematite, which is unattainable by conventional methods. Significantly, our findings reveal the as-synthesized nanocrystals with different predominant facets exhibit facet-dependent OER activities, in agreement with the DFT calculations. By constructing kinetics barriers favorable facets, coupled with strengthening the weak binding with intermediates, the hematite exceedingly outperforms the typically inferior OER behaviors. The accessibility to the specific facets that explicitly govern the OER reactivity in hematite nanocrystals serves as new tunability for the search of high-active catalysts and provides insights into catalyst design strategies.

Experimental Section

Synthesis of Hematite Nanocrystals: For (012)-O facet-dominated α-Fe_2O_3 preparation, an iron foam with a size of 1 cm × 4 cm was immersed into 2×10^{-3} M HCl aqueous solution (20 mL) in a glass bottle and kept at 90 °C for 20 h. Then α-Fe_2O_3 precipitation was obtained by centrifugation at 8000 rpm and washed to a near-neutral condition with deionized (DI) water. The final α-Fe_2O_3 powder was dried at 60 °C. To get (012) facet-dominated α-Fe_2O_3, the as-prepared (012)-O powder was immersed in 0.1 mmol $NaBH_4$ aqueous solution (20 mL) for 10 h at 25 °C, and then collected by centrifugation, washed with DI water for three times, and dried at room temperature.

To prepare (104) facet-dominated α-Fe_2O_3, a modified solvothermal method was adopted.[25] Briefly, 0.15 mmol $Fe(NO_3)_3{\cdot}9H_2O$ was dissolved into 10 mL DI water and ethylene glycol. Then, 15 mmol acetic acid and $NH_3{\cdot}H_2O$ was added into the mixed solution under stirring, respectively. The mixture was transferred into a Teflon autoclave and kept at 200 °C for 15 h. The final precipitate was washed with DI water and ethanol, collected by centrifugation at 8000 rpm, and dried at 60 °C.

The (110) facet exposed α-Fe_2O_3 was synthesized by a modified hydrothermal method.[26] First, 0.03 mmol $FeCl_3{\cdot}6H_2O$ was dissolved into 20 mL DI water and 0.3 mL acetic acid. Then, 5 mmol NaOH was added into the mixed solution under stirring, transferred to a Teflon autoclave, and kept at 180 °C for 10 h. Finally, the powder was centrifuged at 8000 rpm and washed with DI water followed by drying at 60 °C. It is noted that the incubation time for (104) and (110) facet enclosed crystals was optimized to reach a crystal size similar to that of the (012) one.

Computational Methods: All structural relaxations and electronic calculations were carried out based on the spin-polarized DFT as implemented in the Vienna ab initio Simulation Package (VASP). The details are given in the Supporting Information.

Characterization: The SEM images were taken on a field emission SEM (JEOL JSM-7001F). HRTEM images, EDS images, and elemental mapping images were recorded on a JEOL JEM-2100 electron microscope. The XRD patterns were scanned on a Philips X-ray diffractometer with Cu Kα radiation. XPS measurements were performed on a Thermo Scientific ESCA Lab 250 spectrometer and all spectra were corrected using C 1s at 284.6 eV. The EXAFS spectra were recorded in Singapore Synchronic Light Source (SSLS) using transmission mode.

Electrochemical Measurements: To prepare the catalytic electrodes for OER evaluation, 2 mg of the α-Fe_2O_3 powder was dispersed in 0.95 mL ethanol and 50 µL Nafion-117 solution (5%) with ultrasonication treatment for 30 min. Subsequently, 75 µL of the as-prepared ink was dropped onto a carbon fiber paper or Ni foam (1 cm × 1 cm in size

with the edge sealed by epoxy glue), and dried at 80 °C for 12 h. The OER measurements were performed in 1 M NaOH solution in a three-electrode system, with graphite rod as the counter electrode and Hg/HgO as the reference electrode. The potential was calibrated according to the Nernst relation $E_{RHE} = E_{Hg/HgO} + 0.059\ pH + 0.098$. The electrode was performed by CV for 20 cycles with a scan rate of 5 mV s^{-1} before the polarization curves measurement. Linear sweep voltammetry was scanned at 1 mV s^{-1} without iR compensation. The impedance spectroscopy was recorded with the frequency range from 0.1 to 10^5 Hz and the potential at a current density of 5 mA cm^{-2}. The stability test was performed under a galvanostatic mode at current densities from 10 to 20 mA cm^{-2}, and back to 10 mA cm^{-2} with an arithmetic sequence. The turnover frequency was estimated by the equation: $TOF = jM/4Fm$, where j is the current density, F is Faraday constant (96 485 C mol^{-1}), M is the molar mass, m is the loading mass, and 4 is the needed electron number for one molecule of O_2.

Supporting Information

Supporting Information is available from the Wiley Online Library or from the author.

Acknowledgements

The authors acknowledge support from the Ministry of Education, grants R-263-000-C85-112 and R-263-000-D18-112.

Conflict of Interest

The authors declare no conflict of interest.

Keywords

descriptors, facets, hematite, oxygen evolution reaction, reactivity

Received: July 9, 2018
Revised: September 26, 2018
Published online: November 2, 2018

[1] a) L. C. Seitz, C. F. Dickens, K. Nishio, Y. Hikita, J. Montoya, A. Doyle, C. Kirk, A. Vojvodic, H. Y. Hwang, J. K. Norskov, T. F. Jaramillo, *Science* **2016**, *353*, 1011; b) J. H. Montoya, L. C. Seitz, P. Chakthranont, A. Vojvodic, T. F. Jaramillo, J. K. Norskov, *Nat. Mater.* **2017**, *16*, 70; c) S. Gao, Z. Sun, W. Liu, X. Jiao, X. Zu, Q. Hu, Y. Sun, T. Yao, W. Zhang, S. Wei, Y. Xie, *Nat. Commun.* **2017**, *8*, 14503; d) M. Q. Yang, J. Wang, H. Wu, G. W. Ho, *Small* **2018**, *14*, 1703323; e) H. Wu, J. Geng, H. Ge, Z. Guo, Y. Wang, G. Zheng, *Adv. Energy Mater.* **2016**, *6*, 1600794.

[2] a) P. Zhang, L. Li, D. Nordlund, H. Chen, L. Fan, B. Zhang, X. Sheng, Q. Daniel, L. Sun, *Nat. Commun.* **2018**, *9*, 381; b) Z. W. Seh, J. Kibsgaard, C. F. Dickens, I. Chorkendorff, J. K. Norskov, T. F. Jaramillo, *Science* **2017**, *355*, eaad4998.

[3] a) W. T. Hong, M. Risch, K. A. Stoerzinger, A. Grimaud, J. Suntivich, Y. Shao-Horn, *Energy Environ. Sci.* **2015**, *8*, 1404; b) S. Cobo, J. Heidkamp, P. A. Jacques, J. Fize, V. Fourmond, L. Guetaz, B. Jousselme, V. Ivanova, H. Dau, S. Palacin, M. Fontecave, V. Artero, *Nat. Mater.* **2012**, *11*, 802; c) H. Zhong, J. Wang, F. Meng, X. Zhang, *Angew. Chem., Int. Ed.* **2016**, *55*, 9937.

[4] J. Fester, M. Garcia-Melchor, A. S. Walton, M. Bajdich, Z. Li, L. Lammich, A. Vojvodic, J. V. Lauritsen, *Nat. Commun.* **2017**, *8*, 14169.

[5] B. Zhang, X. Zheng, O. Voznyy, R. Comin, M. Bajdich, M. Garcia-Melchor, L. Han, J. Xu, M. Liu, L. Zheng, F. P. Garcia de Arquer, C. T. Dinh, F. Fan, M. Yuan, E. Yassitepe, N. Chen, T. Regier, P. Liu, Y. Li, P. De Luna, A. Janmohamed, H. L. Xin, H. Yang, A. Vojvodic, E. H. Sargent, *Science* **2016**, *352*, 333.

[6] a) Y. Tong, Y. Guo, P. Chen, H. Liu, M. Zhang, L. Zhang, W. Yan, W. Chu, C. Wu, Y. Xie, *Chem* **2017**, *3*, 812; b) H. B. Tao, L. Fang, J. Chen, H. B. Yang, J. Gao, J. Miao, S. Chen, B. Liu, *J. Am. Chem. Soc.* **2016**, *138*, 9978; c) P. Liao, J. A. Keith, E. A. Carter, *J. Am. Chem. Soc.* **2012**, *134*, 13296; d) Z. Lu, H. Wang, D. Kong, K. Yan, P. C. Hsu, G. Zheng, H. Yao, Z. Liang, X. Sun, Y. Cui, *Nat. Commun.* **2014**, *5*, 4345; e) D. A. Kuznetsov, B. Han, Y. Yu, R. R. Rao, J. Hwang, Y. Román-Leshkov, Y. Shao-Horn, *Joule* **2018**, *2*, 225; f) Y. Zhao, C. Chang, F. Teng, Y. Zhao, G. Chen, R. Shi, G. I. N. Waterhouse, W. Huang, T. Zhang, *Adv. Energy Mater.* **2017**, *7*, 1700005; g) B. Klahr, S. Gimenez, F. Fabregat-Santiago, T. Hamann, J. Bisquert, *J. Am. Chem. Soc.* **2012**, *134*, 4294.

[7] J. Suntivich, K. J. May, H. A. Gasteiger, J. B. Goodenough, Y. Shao-Horn, *Science* **2011**, *334*, 1383.

[8] J. Hwang, R. R. Rao, L. Giordano, Y. Katayama, Y. Yu, Y. Shao-Horn, *Science* **2017**, *358*, 751.

[9] I. C. Man, H.-Y. Su, F. Calle-Vallejo, H. A. Hansen, J. I. Martínez, N. G. Inoglu, J. Kitchin, T. F. Jaramillo, J. K. Nørskov, J. Rossmeisl, *ChemCatChem* **2011**, *3*, 1159.

[10] E. Fabbri, A. Habereder, K. Waltar, R. Kötz, T. J. Schmidt, *Catal. Sci. Technol.* **2014**, *4*, 3800.

[11] a) M. Tahir, L. Pan, R. Zhang, Y.-C. Wang, G. Shen, I. Aslam, M. A. Qadeer, N. Mahmood, W. Xu, L. Wang, X. Zhang, J.-J. Zou, *ACS Energy Lett.* **2017**, *2*, 2177; b) Y. Liang, Y. Li, H. Wang, J. Zhou, J. Wang, T. Regier, H. Dai, *Nat. Mater.* **2011**, *10*, 780; c) A. L. Strickler, M. A. Escudero-Escribano, T. F. Jaramillo, *Nano Lett.* **2017**, *17*, 6040; d) J. W. D. Ng, M. García-Melchor, M. Bajdich, P. Chakthranont, C. Kirk, A. Vojvodic, T. F. Jaramillo, *Nat. Energy* **2016**, *1*, 16053; e) Z. Zeng, K.-C. Chang, J. Kubal, N. M. Markovic, J. Greeley, *Nat. Energy* **2017**, *2*, 17070.

[12] a) A. Grimaud, A. Demortiere, M. Saubanere, W. Dachraoui, M. Duchamp, M.-L. Doublet, J.-M. Tarascon, *Nat. Energy* **2017**, *2*, 16189; b) A. Grimaud, O. Diaz-Morales, B. Han, W. T. Hong, Y. L. Lee, L. Giordano, K. A. Stoerzinger, M. T. M. Koper, Y. Shao-Horn, *Nat. Chem.* **2017**, *9*, 457; c) T. Ling, D. Y. Yan, Y. Jiao, H. Wang, Y. Zheng, X. Zheng, J. Mao, X. W. Du, Z. Hu, M. Jaroniec, S. Z. Qiao, *Nat. Commun.* **2016**, *7*, 12876; d) N. Li, D. K. Bediako, R. G. Hadt, D. Hayes, T. J. Kempa, F. von Cube, D. C. Bell, L. X. Chen, D. G. Nocera, *Proc. Natl. Acad. Sci. U.S.A.* **2017**, *114*, 1486; e) S. Yagi, I. Yamada, H. Tsukasaki, A. Seno, M. Murakami, H. Fujii, H. Chen, N. Umezawa, H. Abe, N. Nishiyama, S. Mori, *Nat. Commun.* **2015**, *6*, 8249.

[13] a) X. Zheng, B. Zhang, P. De Luna, Y. Liang, R. Comin, O. Voznyy, L. Han, F. P. Garcia de Arquer, M. Liu, C. T. Dinh, T. Regier, J. J. Dynes, S. He, H. L. Xin, H. Peng, D. Prendergast, X. Du, E. H. Sargent, *Nat. Chem.* **2018**, *10*, 149; b) R. D. L. Smith, C. Pasquini, S. Loos, P. Chernev, K. Klingan, P. Kubella, M. R. Mohammadi, D. Gonzalez-Flores, H. Dau, *Nat. Commun.* **2017**, *8*, 2022.

[14] a) M. S. Burke, L. J. Enman, A. S. Batchellor, S. Zou, S. W. Boettcher, *Chem. Mater.* **2015**, *27*, 7549; b) L. Trotochaud, J. K. Ranney, K. N. Williams, S. W. Boettcher, *J. Am. Chem. Soc.* **2012**, *134*, 17253; c) S. Jung, C. C. L. McCrory, I. M. Ferrer, J. C. Peters, T. F. Jaramillo, *J. Mater. Chem. A* **2016**, *4*, 3068; d) R. Subbaraman, D. Tripkovic, K. C. Chang, D. Strmcnik, A. P. Paulikas, P. Hirunsit, M. Chan, J. Greeley, V. Stamenkovic, N. M. Markovic, *Nat. Mater.* **2012**, *11*, 550.

[15] a) T. Wu, M. L. Stone, M. J. Shearer, M. J. Stolt, I. A. Guzei, R. J. Hamers, R. Lu, K. Deng, S. Jin, J. R. Schmidt, *ACS Catal.* **2018**, *8*, 1143; b) K. A. Stoerzinger, O. Diaz-Morales, M. Kolb, R. R. Rao, R. Frydendal, L. Qiao, X. R. Wang, N. B. Halck, J. Rossmeisl, H. A. Hansen, T. Vegge, I. E. L. Stephens, M. T. M. Koper, Y. Shao-Horn, *ACS Energy Lett.* **2017**, *2*, 876; c) C. Guo, Y. Zheng, J. Ran, F. Xie, M. Jaroniec, S. Z. Qiao, *Angew. Chem., Int. Ed.* **2017**, *56*, 8539; d) R. Gao, J. Zhu, X. Xiao, Z. Hu, J. Liu, X. Liu, *J. Phys. Chem. C* **2015**, *119*, 4516; e) C. W. Tung, Y. Y. Hsu, Y. P. Shen, Y. Zheng, T. S. Chan, H. S. Sheu, Y. C. Cheng, H. M. Chen, *Nat. Commun.* **2015**, *6*, 8106; f) X. Huang, Z. Zhao, J. Fan, Y. Tan, N. Zheng, *J. Am. Chem. Soc.* **2011**, *133*, 4718.

[16] a) C. Li, C. Koenigsmann, W. Ding, B. Rudshteyn, K. R. Yang, K. P. Regan, S. J. Konezny, V. S. Batista, G. W. Brudvig, C. A. Schmuttenmaer, J. H. Kim, *J. Am. Chem. Soc.* **2015**, *137*, 1520; b) K. A. Stoerzinger, L. Qiao, M. D. Biegalski, Y. Shao-Horn, *J. Phys. Chem. Lett.* **2014**, *5*, 1636; c) S. C. Warren, K. Voitchovsky, H. Dotan, C. M. Leroy, M. Cornuz, F. Stellacci, C. Hebert, A. Rothschild, M. Gratzel, *Nat. Mater.* **2013**, *12*, 842; d) Y. Hou, D. Wang, X. H. Yang, W. Q. Fang, B. Zhang, H. F. Wang, G. Z. Lu, P. Hu, H. J. Zhao, H. G. Yang, *Nat. Commun.* **2013**, *4*, 1583; e) C. Gao, Q. Meng, K. Zhao, H. Yin, D. Wang, J. Guo, S. Zhao, L. Chang, M. He, Q. Li, H. Zhao, X. Huang, Y. Gao, Z. Tang, *Adv. Mater.* **2016**, *28*, 6485; f) H. G. Yang, C. H. Sun, S. Z. Qiao, J. Zou, G. Liu, S. C. Smith, H. M. Cheng, G. Q. Lu, *Nature* **2008**, *453*, 638.

[17] a) C. H. Kuo, I. M. Mosa, S. Thanneeru, V. Sharma, L. Zhang, S. Biswas, M. Aindow, S. Pamir Alpay, J. F. Rusling, S. L. Suib, J. He, *Chem. Commun.* **2015**, *51*, 5951; b) Z. Chen, C. X. Kronawitter, B. E. Koel, *Phys. Chem. Chem. Phys.* **2015**, *17*, 29387.

[18] H. X. Lin, Z. C. Lei, Z. Y. Jiang, C. P. Hou, D. Y. Liu, M. M. Xu, Z. Q. Tian, Z. X. Xie, *J. Am. Chem. Soc.* **2013**, *135*, 9311.

[19] J. Ouyang, J. Pei, Q. Kuang, Z. Xie, L. Zheng, *ACS Appl. Mater. Interfaces* **2014**, *6*, 12505.

[20] a) J. Yin, Z. Yu, F. Gao, J. Wang, H. Pang, Q. Lu, *Angew. Chem., Int. Ed.* **2010**, *49*, 6328; b) R. Liu, Y. Jiang, H. Fan, Q. Lu, W. Du, F. Gao, *Chem. - Eur. J.* **2012**, *18*, 8957; c) W. Wu, S. Yang, J. Pan, L. Sun, J. Zhou, Z. Dai, X. Xiao, H. Zhang, C. Jiang, *CrystEngComm* **2014**, *16*, 5566.

[21] H. Wu, T. Zhu, X. Lu, G. W. Ho, *J. Mater. Chem. A* **2017**, *5*, 24153.

[22] H. Wu, X. Lu, G. Zheng, G. W. Ho, *Adv. Energy Mater.* **2018**, *8*, 1702704.

[23] A. K. Patra, S. K. Kundu, A. Bhaumik, D. Kim, *Nanoscale* **2016**, *8*, 365.

[24] T. Odedairo, X. Yan, X. Yao, K. K. Ostrikov, Z. Zhu, *Adv. Mater.* **2017**, *29*, 1703792.

[25] Y. Fu, J. Wang, H.-Y. Yu, X. Li, H. Wang, J.-H. Tian, R. Yang, *Int. J. Hydrogen Energy* **2017**, *42*, 20711.

[26] Y. Zhao, F. Pan, H. Li, T. Niu, G. Xu, W. Chen, *J. Mater. Chem. A* **2013**, *1*, 7242.